The Astrophysical Journal, 756:23 (14pp), 2012 September 1 doi:10.1088/0004-637X/756/1/23

PROBING THE STELLAR HALO OF THE MILKY WAY WITH THE SEKBO RR LYRAE SURVEY

Shaila Akhter, Gary S. Da Costa, Stefan C. Keller, and Brian P. Schmidt
Research School of Astronomy and Astrophysics, Australian National University, Canberra, Australia
Received 2011 December 21; accepted 2012 June 22; published 2012 August 9

ABSTRACT

We investigate the steepening of the power-law slope beyond the Galactocentric radius of $R \sim 45$ kpc in the RR Lyrae (RRL) space density distribution found by Keller et al. They identified 2016 RRL candidates derived from the analysis of archival observations of the Southern Edgeworth-Kuiper Belt Object (SEKBO) survey. Our aim is to verify the completeness of RRLs and ultimately the space density distribution function given by Keller et al. We followed up on a subset of 137 candidates with a range of magnitudes ($V \sim 14$–20) using the Faulkes Telescope (FT) database and confirmed 57 candidates as real RRLs. A cross-match between SEKBO RRL survey and Sloan Digital Sky Survey Data Release-7 (SDSS DR-7) revealed 272 RRL candidates in common. Applying the color selection criteria proposed by Ivezić et al. resulted in 193 likely RRLs. The completeness as a function of magnitude was calculated empirically from the combined set of SEKBO RRL candidates from current FT data, SDSS cross-matched data, and the Prior et al. catalog. This resulted in a spatial density distribution characterized by two power laws with a break radius R within a range between 45 kpc and 50 kpc, similar to the results of Keller et al. We find the power-law slopes for the inner halo as $n_{\text{inner}} = -2.78 \pm 0.02$ and for the outer halo as $n_{\text{outer}} = -5.0 \pm 0.2$.

Key words: Galaxy: halo – Galaxy: structure – stars: Population II – stars: variables: RR Lyrae

Online-only material: color figures, machine-readable table

1. INTRODUCTION

How galaxies like our own Milky Way form is an important question in modern astrophysics. The first proposal was given by Eggen et al. (1962) that the Galaxy formed due to monolithic collapse of an isolated protogalactic cloud. This concept was challenged by Searle & Zinn (1978) with the proposal that the halo was instead constructed from a number of independent infalling protogalactic fragments over an extended period.

These days, many observations suggest that both models have a role to play. Carollo et al. (2007) proposed the dual nature of the halo and showed that the inner halo ($R \sim 10$–15 kpc) is nonspherically distributed and exhibits highly eccentric orbits, prograde rotation, and metallicities [Fe/H] ~ -1.6. The outer halo, on the other hand, has a much more spherical spatial distribution and is dominated by a uniform distribution of eccentricities, highly retrograde rotation, and metallicities [Fe/H] ~ -2.2. The results of Carollo et al. (2007) were later refined and extended by Carollo et al. (2010). However, Schönrich et al. (2011) criticized the above results and demonstrated that the retrograde signature of the outer halo population may be due to incorrect distance calculations. Beers et al. (2012), on the other hand, confirmed the findings of Carollo et al. (2007, 2010) by comparing their distance calculations with the recommended relations given by Ivezić et al. (2008) and An et al. (2011).

The findings of Carollo et al. (2007, 2010) are consistent with those of Bell et al. (2008), Kinman et al. (2007), and Carney (1999), who suggested that the inner halo was formed from rapid collapse and the outer halo from many accretion events. Such concepts are in line with current ΛCDM cosmological models, which predict that the formation of all galaxies is a consequence of baryon dissipations within massive dark matter halos formed from many merging and accretion events (e.g., Abadi et al. 2006; Bullock & Johnston 2005).

Halo tracers are the most reliable means to provide valuable information on the Galaxy's formation, as they probe the dynamics of old stellar populations. Among various halo tracers, RRLs are significantly useful as they are standard candles, are metal poor and very old, and are relatively common and easy to recognize because of their characteristic colors and light curves with large amplitudes and short periods.

Study of the stellar space density distribution in the halo gives us a clue to the formation of our halo. Saha (1985) noticed that the RRL density profile steepens rapidly beyond Galactocentric radii of 25 kpc. Since then, various observational studies have found this break in the power-law slope of space density distributions at large galactic radii for various tracers like RRLs, globular clusters, and main-sequence turnoff (MSTO) stars (Deason et al. 2011; Sesar et al. 2010, 2011; de Jong et al. 2010; Watkins et al. 2009; Bell et al. 2008; Miceli et al. 2008; Wetterer & McGraw 1996). However, this slope steepening is absent in the distribution of blue horizontal branch (BHB) stars obtained by De Propris et al. (2010), who found a rather smooth stellar distribution in the halo. Theoretical studies also predict that the slope of the mass density profile decreases at large galactic radii, $R > 30$ kpc (Font et al. 2011).

The current study is based on the SEKBO RRL survey (Keller et al. 2008, hereafter K08). The SEKBO (Southern Edgeworth-Kuiper Belt Object) survey (Moody et al. 2003) was a three epoch (second epoch separated by ∼4 hr from the first one, the third epoch taken 1–7 days later), two color imaging survey of a 10° band centered on the ecliptic designed to search for trans-Neptunian objects. K08 used images from this survey to identify 2016 RRL candidates over an area of 1675 deg^2. They used simulations of their data set to interpret their completeness as a function of magnitude. They found the power-law slope, n, of the RRL space density distribution as -2.48 ± 0.09 for the candidate RRLs between 10 kpc $< R <$ 45 kpc. Whereas beyond $R = 45$ kpc this slope was steeper, $n = -5 \pm 0.3$. However, K08 chose not to interpret the increased radial drop off beyond $R = 45$ kpc pending confirmation of their completeness as a function of magnitude.

In this paper, we investigate the validity of the broken power law found by K08. Section 2 describes the observations taken and how they were reduced using an automated pipeline to select variables. Section 2 also illustrates the selection of RRLs among the variables. The photometric calibration of these RRLs and the corresponding completeness of the current survey are explained in Section 3. A cross-match between the SEKBO RRL survey and SDSS DR-7 aided in an independent check of the outcome. This is expounded in Section 4. Section 5 compares and combines the results from the current followup, SDSS DR-7 cross-match and the Prior et al. (2009) study into a single best estimate of completeness as a function of $V_{\rm SEKBO}$. Section 6 presents the space density distribution of confirmed RRLs. Finally, the results are discussed in Section 7. Briefly, we find that the power-law slope of the space density distribution of the SEKBO RRLs steepens from the inner to the outer halo beyond 45 kpc consistent with the results of K08.

2. OBSERVATIONS AND DATA REDUCTION

2.1. The Data

For the current investigation, 207 fields containing SEKBO candidates with magnitudes $14 < V < 20$ were followed up photometrically using images from the database of Faulkes telescopes (North and South) observations. The fields cover all R.A. and $-28° > \text{decl.} > 20°$. Data were taken, using the Bessell-V filter, from 2008 September to 2010 June in queue-scheduled mode as a fill-in between larger programs. Consequently, the observations were taken at irregular time intervals and many objects have images separated by 3–10 months. Each field studied has 3–30 observations with seeing ∼0.8–3.5 arcsec. Exposure times varied from 20 s for the brighter objects to 300 s for the faintest.

2.2. Construction of an Automated Pipeline for Photometric Data Reduction and Analysis: Variable Selection

In this section, we explain how we reduced raw input data to determine variables. We constructed an automated pipeline that performs aperture photometry on input images and produces unphased light curves for SEKBO RRL candidates. This pipeline is mainly constructed using IRAF and Python. The back-end database is stored in a MySQL database environment.

The pipeline takes input images (flat fielded and bias subtracted) collected from the Faulkes telescope (hereafter FT) database and calculates the Heliocentric Julian Date (HJD) for each image. It selects images as "good data" if the seeing <2.6 arcsec and sky background <1500 counts. An appropriate reference image is then selected for each field according to the best signal-to-noise ratio (S/N). This S/N depends on the fluxes of the weighted mean instrumental magnitudes of all frames for each field. The pipeline detects objects (i.e., stars) on the reference frame and on other frames using IRAF task *daofind*. Aperture photometry is then performed on these objects with IRAF task *phot* on all frames, producing magnitudes and associated errors for all the objects. For each field, the pipeline also calculates the differential magnitudes and errors for each image relative to their corresponding reference image.

The rationale for generating unphased light curves was to determine whether an object is a possible variable or a non-variable. The pipeline finds the candidate variables if variability ratio >3 (variability ratio is the ratio of the standard deviation of the relative (instrumental) magnitudes at various epochs to the mean of the errors associated with the differential magnitudes).

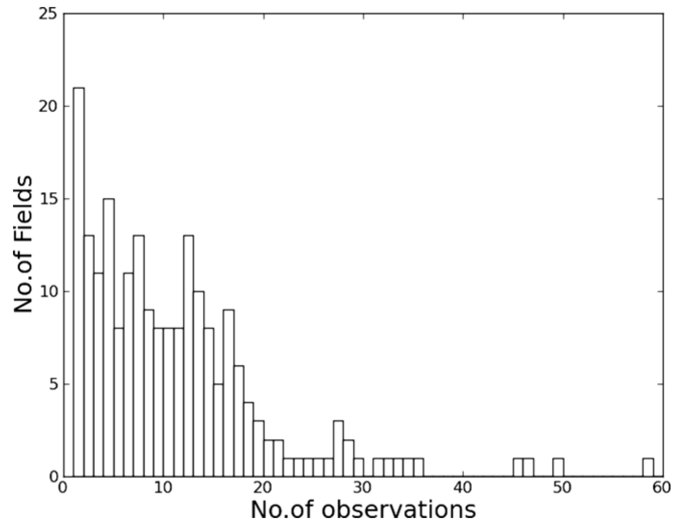

Figure 1. Distribution of the number of observations per field for the sample of 207 fields.

In the current work, 2228 images representing 207 objects were selected as good data. The number of frames obtained for each object is solely controlled by the Faulkes scheduling process. The histogram in Figure 1 shows the number of observations per field. As in the figure, 34 objects have either one or two frames, which is insufficient to determine their variability. Therefore, these 34 objects were dropped and the remaining 173 were selected for further analysis. The pipeline resulted in 108 variables and 65 non-variables. To verify the efficiency of the pipeline, we inspected the light curves of the non-variables visually and found 4 out of 13 candidates having $2.2 < \text{variability ratio} < 3$ are actually likely variables. Another six have insufficient data (⩽5 images) and were discarded from the final completeness profile calculation (Section 3.4) as they need more observations to confirm their nature. The remaining three were indeed non-variables. We finally obtained 112 candidates as variables, though not all RRLs.

2.3. Phased Light Curves: Selection of RR Lyraes

Once objects are detected as variables, they need to be classified in order to confirm them as RRLs. For this purpose, data (HJD of observations, instrumental V-band (differential) magnitudes and their errors) for the unphased light curves of the variables were collected from the pipeline database. As a first check, IRAF task *pdm* (phase dispersion minimization) is used to estimate the variability, amplitude, and period. Then based on the possibility of the variables being of type RRL, eclipsing binary, or Algol, Andrew Layden's period fitting (Layden et al. 1999) and light curve fitting routines (Layden 1998) are used to predict their classification more accurately. The period–amplitude relationship exhibited by RRab type stars, where period increases with a decrease in amplitude, was also employed in the period selection. Any varying object whose period could not be determined was tagged as unclassified variable.

The Layden routines use 10 templates consisting of five RRab, two RRc, one sine, one eclipsing binary, and one Algol light curves. In the period fitting routine, it generates a period curve for a variable star by calculating the chi-square minima of the observed data using the templates over a range of periods. This plot enables us to choose the best possible period from the lowest chi-square values. Using this period in the light curve fitting routine, the variable is determined as an RRL or

Table 1
Summary of SEKBO RRL Candidate Classification

Classification	Number of Objects
Total objects	207
Total objects with ⩽2 images	34
Total objects with >2 images	173
Non-variables	55
Need more observations	36
Total variables	82
RRab	45
RRc	12
Eclipsing binaries	17
Algol	2
Undefined variables	6

non-RRL through template matching (according to the amplitude, period, and shape of the phased light curve). Eleven objects with up to eight images show good fits with more than one standard light curves, including RRLs, with Andrew Layden's light curve fitting routines. For these objects we need more observations to confirm their classification. It is important to note that objects were defined as variables with at least three observations, whereas, to confirm a variable to be an RRL, we need at least five observations. There are 19 variables with <5 images, for which we need more observations to confirm their nature. Consequently, we have discarded these 30 unclassified variables from the completeness profile calculation (Section 3.4). Overall in this process, we confirmed 45 RRab, 12 RRc, two Algol, 17 eclipsing binaries, and six undefined variables (non-RRLs). The RRc stars have periods of ∼0.3–0.5 days, whereas periods for RRab vary from ∼0.5 to 1.2 days; typical period uncertainties ∼0.001 days. Our findings are summarized in Table 1.

3. PHOTOMETRIC CALIBRATION OF RR LYRAE STARS

3.1. Standardized Instrumental Magnitudes of RR Lyraes

A photometric night was sought to calibrate the instrumental magnitudes of the confirmed RRLs. A night, preferably common to more than one RRL, is first selected using the AAT diary.[1] The selection criteria were: (1) seeing <3 arcsec, (2) the sky cloud-free for the UT time of the corresponding RRL star observations, and (3) the standard stars were also observed in a cloud-free window.

From the FT database, images were collected for available standard stars of different fields for the selected night. For each field, growth curves (aperture versus magnitude) were plotted for the aperture photometry, from which total magnitudes for each of the stars were calculated. Knowing their exposure time (EXPTIME), extinction coefficient (k_v), and airmass (X), their instrumental V magnitude ($V_{\rm Ins}$) were calculated. Using Landolt (1992) and Stetson's[2] photometric catalogs, $V_{\rm Ins}$ are compared with standard magnitudes for the individual standard stars. A linear fit to $(B-V)$ versus $(V_{\rm Ins}-V)$ yielded the slope (Y) and the zero point (ZP).

The same procedure is repeated for other standard field(s) from the same night. If the slopes and the zero points from the different standard fields are consistent (e.g., difference between ZPs < 0.1), the night is determined as a photometric night. A linear fit for the combined points, $(B-V)$ versus $(V_{\rm Ins}-V)$, for all the fields then gives the final slope and the zero point to be used to standardize the RRL(s).

Then an image of an RRL for the corresponding photometric night was selected. Using IRAF task *phot*, aperture photometry was performed on the RRL as well as on a few non-variable stars with a particular aperture ($A_{\rm p}$). The aperture magnitude of the RRL was corrected ($A_{\rm corr}$) to total magnitude using bright non-variable stars on the same image. Then from the two equations given below, the standard magnitude $V_{\rm standard}$ of the RRL for the photometric night was calculated:

$$v = \text{magnitude(through } A_{\rm p}) + 2.5\log(\text{EXPTIME}) - k_{\rm v}X - A_{\rm corr}, \quad (1)$$

$$v - V_{\rm standard} = Y * (B-V) + \text{ZP}. \quad (2)$$

The value of $(B-V)$ for RRLs is ∼0.2 and the slope Y was found as 0.057 ± 0.002 mag mag^{-1}. We chose to neglect the color term as the effect of $Y * (B-V)$ on the magnitude is small. The offsets between the uncorrected instrumental V magnitudes ($V_{\rm insRRL}$) of confirmed RRLs from the pipeline database and $V_{\rm standard}$ were calculated and applied to all $V_{\rm insRRL}$ from the different images for that RRL. Layden's programs (Section 2.2) were then again used to generate the phased light curve of the RRL with its standard magnitudes (an example is shown in Figure 2). The confirmed RRLs and their various parameters are listed in Table 2 and the complete set of light curves is given in the Appendix (see Figure A1). In the table, $N_{\rm Obs}$ is the number of observations for each RRL, $V_{\rm SEKBO}$ is the magnitude from SEKBO RRL survey, and $V_{\rm FT}$ is the standardized magnitude from the current follow-up.

Some RRLs have light curves with periodic amplitude and/or phase modulation, on a timescale of tens of days. This phenomenon is called the Blazhko effect after one of its discoverers (Blažko 1907). We found five Blazhko RRLs (104638.2589, 117602.795, 110716.1021, 116920.426, and 116385.432), illustrated in Figure 3.

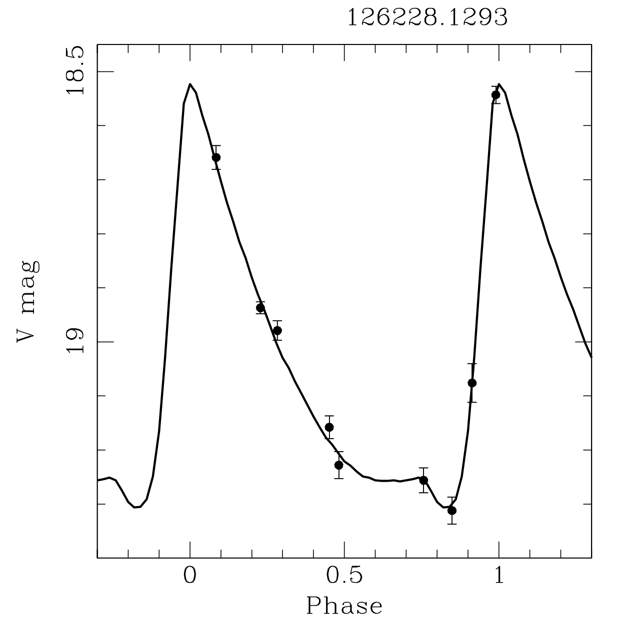

Figure 2. Light curve of an RRab type star (126228.1293) after photometric calibration: $V = 19.017$, period = 0.577 days, and amplitude = 0.783 mag. The solid circles are the observations and the solid line is the best-fit template light curve from Layden (1998).

[1] http://site.aao.gov.au/AATdatabase/diary/diary.html
[2] This research used the facilities of the Canadian Astronomy Data Centre operated by the National Research Council of Canada with the support of the Canadian Space Agency.

Table 2
Positions and Derived Parameters for Confirmed RR Lyraes

Star ID	R.A. (J2000.0)	Decl. (J2000.0)	Star Type	N_{Obs}	V_{SEKBO}	V_{FT}	V_{Diff}	Period (days)	A_V
113345.875	21 39 27.80	−17 17 45.94	RRab	13	17.98	17.91	0.070	0.527	1.155
115133.1186	21 31 17.34	−11 49 33.34	RRc	14	16.87	16.87	0.000	0.406	0.468
124901.470	21 44 12.87	−20 34 55.42	RRab	14	17.34	17.42	−0.077	0.535	1.108
125062.1184	20 51 05.62	−21 47 45.34	RRab	16	17.84	17.87	−0.028	0.472	1.335
125853.3464	20 56 21.46	−13 48 14.74	RRab	10	19.01	18.80	0.210	0.522	0.884
126046.1166	21 44 48.81	−18 04 55.99	RRc	14	17.35	17.42	−0.069	0.382	0.376
126228.1293	22 17 39.34	−16 57 42.84	RRab	09	19.05	19.02	0.030	0.577	0.783
126446.3248	21 52 19.27	−18 09 03.58	RRab	12	19.63	19.50	0.130	0.624	1.081

(This table is available in its entirety in a machine-readable form in the online journal. A portion is shown here for guidance regarding its form and content.)

Table 3
RRL Completeness Factors for Various Surveys in Different *V* Magnitude Bins

(1)	(2)	(3)	(4)	(5)	(6)	(7)	(8)	(9)	(10)	(11)
						Data Set				
Magnitude Bins	K08 Adopted	Current Follow-up			Prior et al. (2009)			Combined		
	C (%)[c]	Cand.[a]	RRLs[b]	C (%)[c]	Cand.[a]	RRLs[b]	C (%)[c]	Cand.[a]	RRLs[b]	C (%)[c]
14–15	60	04	00	0.00	...	...	...	04	00	0.00
15–16	60	13	04	31 ± 18	16	09	56 ± 23	23	10	43 ± 16
16–17	60	13	06	46 ± 23	21	18	86 ± 28	32	22	69 ± 19
17–18	60	41	34	83 ± 19	53	45	85 ± 17	82	69	84 ± 14
18–19	28	43	07	16 ± 07	02	00	0.00	45	07	16 ± 06
19–20	15	23	06	26 ± 12	02	01	50 ± 61	23	06	26 ± 12

Notes.
[a] Number of SEKBO RRL candidates.
[b] Number of confirmed RRLs.
[c] Completeness fraction of RRLs in %.

3.2. Comparison between the Photometry of the Current Follow-up and That of the SEKBO RRL Survey

Figure 4 depicts the difference between magnitudes from the SEKBO RRL survey (V_{SEKBO}) and the FT follow-up (V_{FT}; see Table 2). The small mean magnitude difference (−0.05 mag) verifies the K08 photometry and hence the distances calculated from these magnitudes are reliable. The standard deviation of the differences in Figure 4, which represents the sum of our and K08 errors, is 0.158 mag. We estimate our errors as ∼0.03–0.05 mag suggesting that the actual uncertainty in the K08 mean magnitudes is ∼0.10–0.12 mag. This is not surprising given that K08 typically only had three measurements from which to determine mean magnitudes for the variables.

3.3. Survey Completeness from FT Data

The completeness of the survey needs to be estimated before the spatial distribution of RRLs can be discussed. The completeness is measured by the fraction of true RRL recovered as a function of apparent magnitude. Columns 3–5 in Table 3 illustrate the completeness (in percentage) obtained from our current follow-up in various magnitude bins. We give also the completeness fractions estimated by K08 in Column 2 of Table 3. These have been estimated from a simulation that produces similar power-law slopes for the spatial number distribution as found by K08, as individual completeness factors for different magnitude bins were not explicitly given in K08.

Similar work to that here has been done by Prior et al. (2009) where they followed up a subset of SEKBO RRL candidates photometrically. The completeness from the Prior study (Columns 6–8) and from the combined data set of current FT and Prior et al. (2009; Columns 9–11) are also given in Table 3.

It is notable from Table 3 that the completeness profile obtained from the current follow-up is similar to that of K08 in all the magnitude bins. The apparent small completeness fraction 31% ± 18% (Figure 5(a)) in our study for $15 < V < 16$ is consistent with 60% (as estimated by K08) at the $<2\sigma$ level. In this magnitude range, out of 13 SEKBO candidates, four were found as RRLs, two as eclipsing binaries, three as undefined variables, and the others as non-variables. We note here that for the $15 < V < 16$ bin, Prior et al. (2009) found a completeness (Figure 5(b)) of 56% ± 23% and the combined data set results in completeness (Figure 5(c)) of 43% ± 16% (out of 23 SEKBO candidates, 10 found as RRLs, eight as non-RRL variables, and the others as non-variables). This is now consistent with K08 findings within the 1σ level.

We note also that we found 0% completeness for $14 < V < 15$. Out of four candidates in this magnitude range, three were found as EBs and one as non-variable. Prior et al. (2009) did not follow up any candidate in this magnitude range. For four candidates and the K08 60% completeness, we expect to find $2 \pm \sqrt{2}$ real RRLs. Therefore our finding of no RRLs is consistent at $<2\sigma$ level. Clearly follow-up of more candidates is needed to have a better estimation of the completeness fraction for this magnitude bin.

It is evident from the data shown in Figure 5 that the number of confirmed RRLs drops to ∼25% beyond $V = 18$ mag.

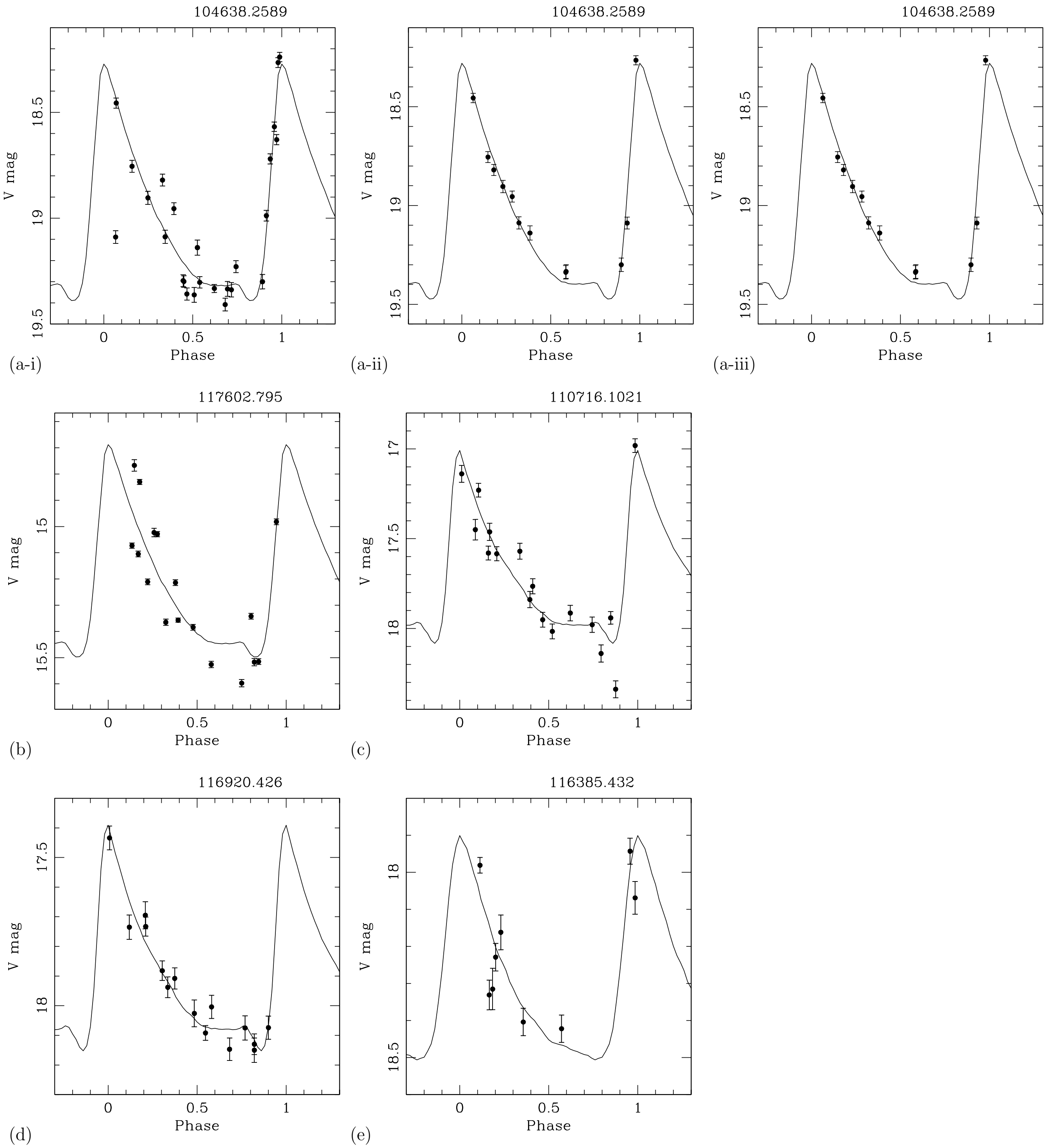

Figure 3. RR Lyraes with Blazhko effect. (a-i) Star ID: 104638.2589, $V = 18.958$, period = 0.523 days, amplitude = 1.117 mag, 25 observations over 364 days in two sets separated by 306 days. (a-ii) Same star as (a-i), $V = 19.008$, period = 0.521 days, amplitude = 1.193 mag, 12 observations over 27 days in 2009. (a-iii) Same star as (a-i), $V = 18.988$, period = 0.521 days, amplitude = 1.184 mag, 13 observations over 31 days in 2010. (b) Star ID: 117602.795, $V = 15.197$, period = 0.525 days, amplitude = 0.809 mag, 17 observations spanning 64 days. (c) Star ID: 110716.1021, $V = 17.682$, period = 0.586 days, amplitude = 1.074 mag, 17 observations over 129 days. (d) Star ID: 116920.426, $V = 17.878$, period = 0.574 days, amplitude = 0.761 mag, 15 observations spanning 114 days (six observations over 12 days and nine over 27 days). (e) Star ID: 116385.432, $V = 18.284$, period = 0.547 days, amplitude = 0.605 mag, nine observations spanning 113 days in two sets separated by 75 days.

4. CROSS-MATCH BETWEEN SEKBO RR LYRAE SURVEY AND SDSS DR-7

4.1. Selection Process

A cross-match between SEKBO RRL candidates and the SDSS DR-7 database revealed 272 SEKBO RRL candidates in common. Ivezić et al. (2005) proposed how to select RRL stars using single-epoch data from the SDSS DR-1 database. They used a complete sample of RRL stars discovered by the Quasar Equatorial Survey Team (QUEST) survey and proposed some selection criteria. Later, Sesar et al. (2010) proposed some modifications to find RRLs in SDSS Stripe 82. Combining their

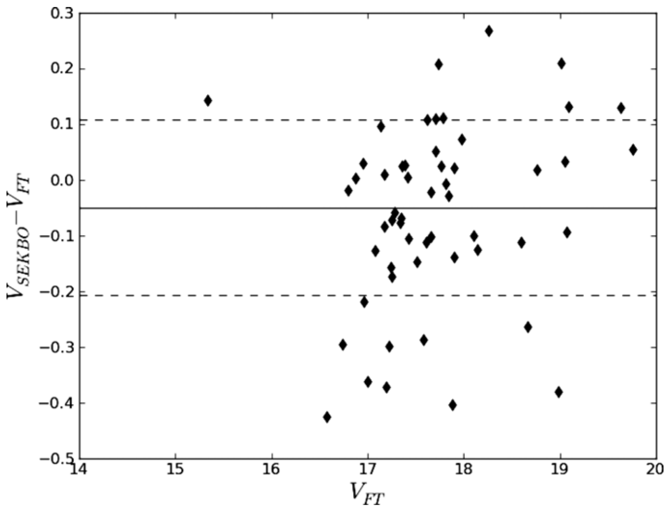

Figure 4. Magnitude difference between the magnitudes of SEKBO RRL candidates given in the SEKBO catalog, $V_{\rm SEKBO}$, and the mean magnitudes of confirmed RRLs determined here, $V_{\rm FT}$, as a function of $V_{\rm FT}$. The solid line indicates the mean magnitude difference and the dashed lines indicate its associated 1σ dispersion.

selection processes, the following criteria have been used to select RRLs from the cross-match:

$$14 < r < 20, \quad (3)$$

$$0.75 < (u - g)_0 < 1.45, \quad (4)$$

$$-0.25 < (g - r)_0 < 0.4, \quad (5)$$

$$-0.2 < (r - i)_0 < 0.2, \quad (6)$$

$$-0.3 < (i - z)_0 < 0.3, \quad (7)$$

$$D_{ug}^{\rm Min} < D_{ug} < 0.35, \quad (8)$$

$$D_{gr}^{\rm Min} < D_{gr} < 0.55, \quad (9)$$

where

$$D_{ug} = (u - g)_0 + 0.67(g - r)_0 - 1.07, \quad (10)$$

$$D_{gr} = 0.45(u - g)_0 - (g - r)_0 - 0.12. \quad (11)$$

Among these color criteria, Equations (3)–(7) were given by Sesar et al. (2010) and Equations (8)–(11) by Ivezić et al. (2005). The colors were dereddened using Schlegel et al. (1998, Table 6).

D_{ug} and D_{gr} represent the positive and negative slopes between $(u - g)$ and $(g - r)$ color–color space such that chosen RRLs are free from significant sources of contamination (Ivezić et al. 2005).

Following the above criteria and choosing $D_{ug}^{\rm Min} = -0.05$ and $D_{gr}^{\rm Min} = 0.06$ to get a large success rate (e.g., it gives 100% success rate for QUEST survey RRLs; Vivas et al. 2004; Ivezić et al. 2005; Watkins et al. 2009), 193 of 272 candidates are possible RRLs.

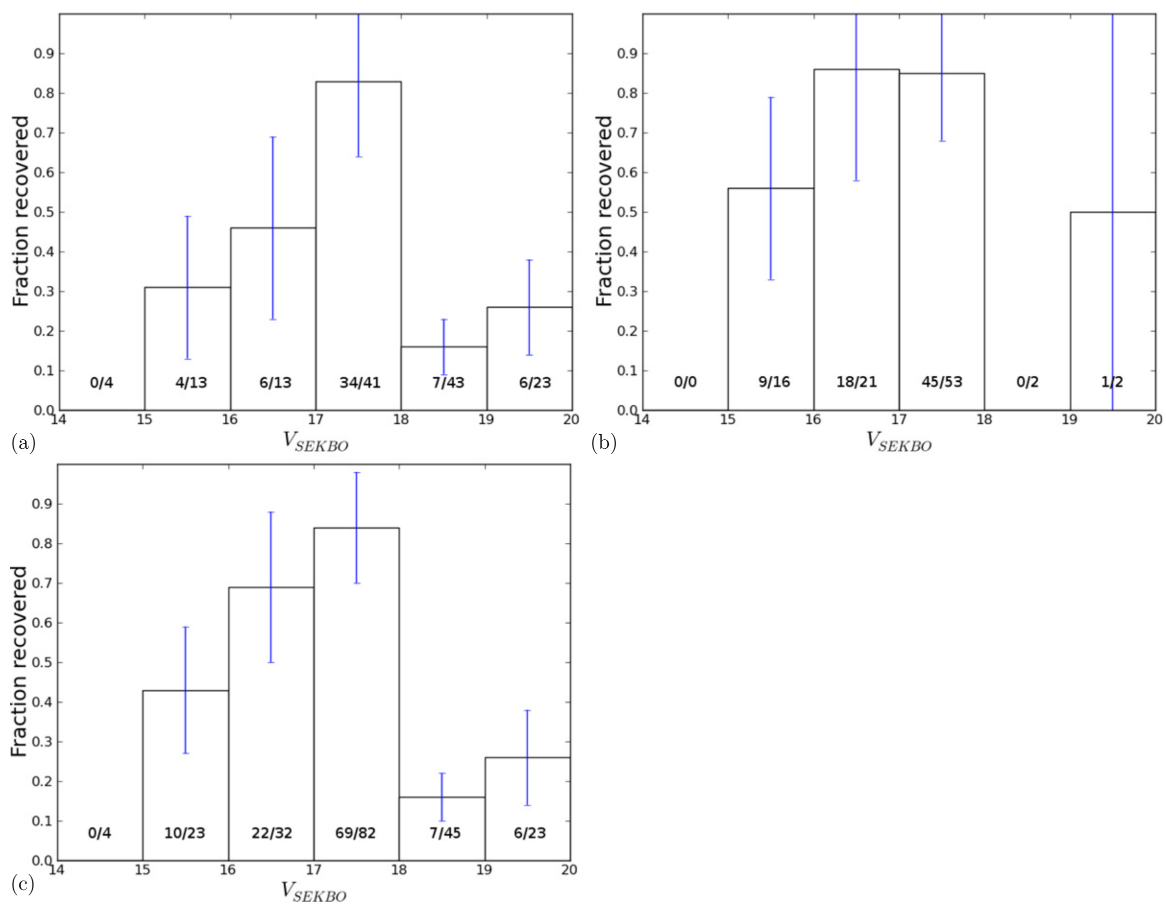

Figure 5. Completeness profile of RRL variables as a function of $V_{\rm SEKBO}$ magnitude: (a) for current FT data set, (b) for Prior et al. (2009) data set, and (c) for the combined data set. Number of RRLs/number of SEKBO candidates are indicated in each magnitude bin. The errors are calculated assuming Poisson statistics.

(A color version of this figure is available in the online journal.)

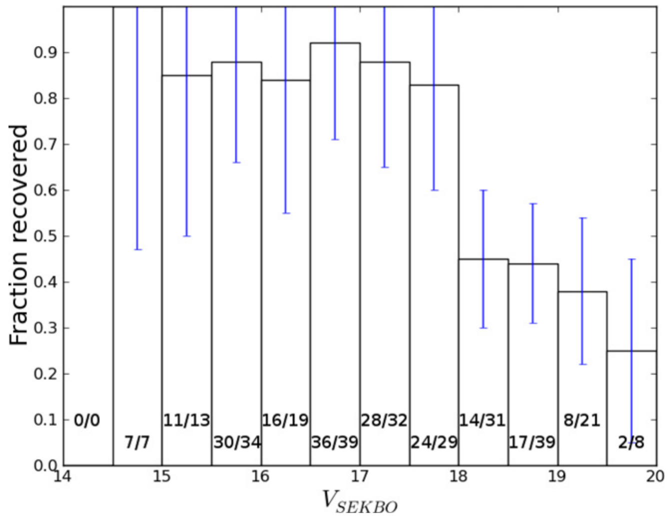

Figure 6. Completeness profile for the 193 likely RRLs out of 272 candidates resulting from the cross-match between the SDSS data (DR-7) and the 2016 SEKBO RRL candidates (K08) as a function of $V_{\rm SEKBO}$ magnitude. The errors are calculated assuming Poisson statistics.

(A color version of this figure is available in the online journal.)

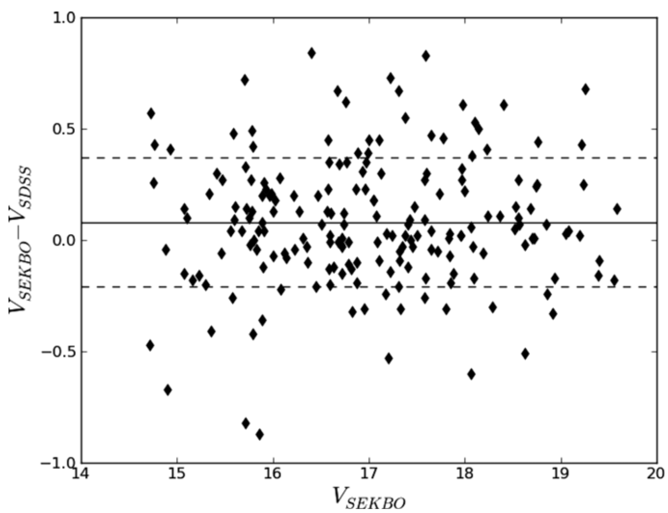

Figure 7. Difference between the magnitudes given in the SEKBO catalog, $V_{\rm SEKBO}$, and $V_{\rm SDSS}$, the magnitude derived from the g magnitude of the color-selected matching candidates as a function of $V_{\rm SEKBO}$. The solid line indicates the mean magnitude difference and the dashed lines indicate its associated 1σ dispersion.

4.2. Completeness of the Selection Process

The typical completeness profile for these RRL candidates, as a function of $V_{\rm SEKBO}$ magnitude, is shown in Figure 6. It is clear from the plot that, for $V < 18$, completeness fraction $\geqslant 85\%$ and drops to $\sim 45\%$ beyond this limit.

For consistency, the g magnitudes have been converted to V magnitudes using the following equation for metal-poor Population II stars (Jordi et al. 2006):

$$V - g = (-0.569 \pm 0.007) * (g - r) - (0.021 \pm 0.004). \quad (12)$$

The mean difference $V_{\rm SEKBO} - V_{\rm SDSS}$ for the 193 RRL candidates is 0.08 mag with a standard deviation of 0.29 mag (Figure 7). The small mean magnitude difference again suggests that the $V_{\rm SEKBO}$ magnitudes are reliable. However, the standard deviation of 0.29 mag is significant, but not surprising given that the SDSS g magnitudes are single-epoch data.

Table 4
Efficiency of the Color-selection Process for $V > 18$

Magnitude Bin	$n_{\rm RRLs}$[a]	$n_{\rm Candidates}$[b]	Completeness[c]
SDSS			
(i) With 0.5 mag bin			
18.0–18.5	14	31	0.36 ± 0.13
18.5–19.0	17	39	0.35 ± 0.11
19.0–19.5	08	21	0.30 ± 0.14
19.5–20.0	02	08	0.20 ± 0.17
SDSS			
(ii) With 1 mag bin			
18.0–19.0	31	70	0.35 ± 0.08
19.0–20.0	10	29	0.28 ± 0.11
Combined			
(iii) With 1 mag bin			
18.0–19.0	07	45	0.16 ± 0.06
19.0–20.0	06	23	0.26 ± 0.12

Notes.
[a] Number of RRLs (i), (ii) in SDSS color-selected RRL window, and (iii) found by the combined data set of FT and Prior et al. (2009).
[b] Number of SEKBO candidates (i), (ii) in SDSS data set, and (iii) in the combined data set.
[c] Completeness fraction of RRLs (i), (ii) in SDSS color-selected RRL window with 80% success rate, and (iii) in the combined data set.

4.3. Efficiency of the Selection Process

The color selection process given by Ivezić et al. (2005) with the values $D_{ug}^{\rm Min} = -0.05$ and $D_{gr}^{\rm Min} = 0.06$ provided 100% success rate for QUEST survey RRLs with 6% efficiency. While on the contrary, Sesar et al. (2010) constructed an RRL template using multiple observations, analyzed the template behavior and performed template fitting along with the use of an extended color range for the initial selection and found RRLs with almost 100% success rate and 100% efficiency.

Matching SDSS and SEKBO data sets we find 272 stars in common and of these 193 fall in the SDSS color-selected RRL window. The fraction of SEKBO candidates in this RRL window is shown as a function of V in Figure 6. This fraction is almost constant for $V < 18$ and falls for fainter magnitudes. Indeed for $V < 18$ we have 152 SEKBO stars in the SDSS RRL window versus 173 total, so the success rate is $152/173 = 88\% \pm 10\%$. The question then is what fraction of 193 SDSS candidates are really RRLs. To address this, we looked at the combined data set from Prior et al. (2009) and current FT catalog for stars in SDSS data set that have been confirmed as RRLs. For $V < 18$, we have 15 objects that are in the SDSS RRL window and of these 12 objects are confirmed RRLs, i.e., the efficiency is $12/15 = 80\% \pm 31\%$. Consequently, the SDSS match-up predicts for the SEKBO candidates that the number of true RRLs is: $0.88 \pm 0.10 * 0.80 \pm 0.31 = 0.70 \pm 0.28$. This is consistent with the combined data set of FT and Prior et al. (2009), i.e., for $V < 18$, the efficiency is 0.71 ± 0.09. Then applying the same 80% success rate to the fainter bins gives the results shown in Table 4. It is evident from this table that the efficiency of the SDSS color selection process in finding real RRLs is in agreement with that of the combined set to within $<2\sigma$.

The matching of the candidates that have been followed up here and in Prior et al. (2009) with the SDSS also confirmed 1 RRL and 20 non-RRLs from the remaining non-RRL SDSS candidates. This single RRL identified in the non-RRL window has slightly smaller $(u - g)_0 (= 0.658)$ and small

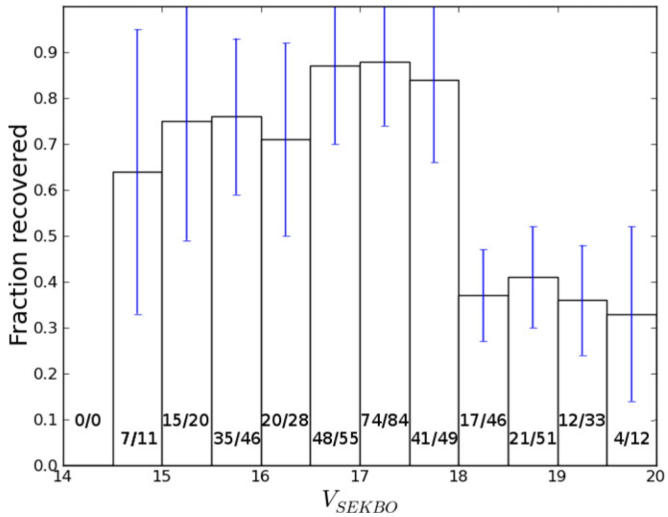

Figure 8. Completeness profile for 294 RRLs out of 435 candidates in the SEKBO RRL survey as a function of $V_{\rm SEKBO}$ magnitude from the combined data set. The errors are calculated assuming Poisson statistics.

(A color version of this figure is available in the online journal.)

$D_{ug}(= -0.481)$, while the star follows the other color criteria. Its nonselection is likely due to the high reddening ($E(u-g)_0 = 1.232$ and $E(g-r)_0 = 0.942$) of this star. The light curve found for this star has a perfect RRab shape, period, and amplitude. Overall this demonstrates that the color selection criteria are 95% ± 30% efficient in finding non-RRLs.

To summarize, in this process with ∼100% success rate and 80% efficiency, we derived completeness in percentages for the SEKBO survey as 70% ± 28%, 35% ± 8%, and 28% ± 11% for $V < 18$, $18 < V < 19$, and $19 < V < 20$, respectively.

5. ADOPTED COMPLETENESS AS A FUNCTION OF V

Combining the three different catalogs of current FT, Prior et al. (2009) and SDSS DR-7, we get 435 different SEKBO RRL candidates, which result in 294 genuine RRLs (with ∼70% efficiency for SDSS stars and 100% efficiency for the other two catalogs). The completeness profile for this combined set (Figure 8) is in good agreement with what K08 estimated, i.e., for $14 < V < 18$ the completeness is ∼70% and for $V > 18$ it reduces to zero by $V \sim 20$.

6. SPACE DENSITY DISTRIBUTION

K08 derived the spatial distribution of RRLs in the halo by considering a Monte Carlo derived RRab completeness profile. This assumed ∼60% completeness for $V < 18.5$, falling to a mean completeness of 25% by $V = 19.5$. They then found the power-law slopes for the inner and the outer halos as -2.48 ± 0.09 and -5.0 ± 0.3, respectively, with the break radius at $R = 45$ kpc.

We calculated the spatial density of RRLs as a function of Galactocenric radius following similar methods to that discussed by K08. We assume for a spherical halo, that the density varies as a function of Galactocentric distance as a power law,

$$\rho(R) = \rho_0 (R/R_0)^n, \quad (13)$$

where ρ_0 is the local space density of RRLs and R_0 is the solar radius.

Wetterer & McGraw (1996) described the density as a function of Galactocentric distance by the following equation:

$$\rho(R) = \frac{1}{4\pi R^2 f(R)} \frac{dN}{dR}, \quad (14)$$

where R is the Galactocentric distance, N is the number of RRL as a function of distance, and $f(R)$ is the fraction of the total halo volume at R sampled by the survey. $f(R)$ varies as a function of Galactocentric radius and was calculated numerically for each field.

To achieve the effective halo volume sampled by each individual field, we then multiplied each $f(R)$ by the completeness profile of RRLs (Section 5) as a function of radius. The total volume is the sum of $f(R)$ for all fields. To quantify the number gradient dN/dR, we plotted the cumulative distribution of candidates, i.e., the cumulative number of RRLs as a function of Galactrocentric distance R and then calculated dN/dR numerically from it. Finally, the local space density of RRLs was calculated using Equation (14).

From the combined data set (Figure 8) we find that the completeness for the brighter magnitudes, and therefore closer distances, is 70% but it drops significantly for the fainter magnitudes and larger distances. In practice, this drop off can occur between $V = 17$ and 18.5 reaching 0% completeness at $V \sim 20$. Bearing this in mind, we took the completeness as 70% for $14.5 < V < V_{\rm Break}$ and decreasing to 0% at the faintest magnitude $V_{\rm Edge}$. We then varied $V_{\rm Break}$ from 17 to 18.5 with 0.5 mag bins and $V_{\rm Edge}$ from 20.2 to 20.8 with 0.1 mag bins. For each $V_{\rm Break}$, we found seven different models corresponding to different $V_{\rm Edge}$ values. We further considered four combination models from each such seven models where the completeness decreases in a nonlinear fashion. In this way, we found 44 different models (Figures 9(a) and (c) showing the two boundary models) of completeness profiles and calculated the space density distribution for each of them. We then calculated the weighted mean and the weighted standard deviation of all the power-law slopes.

As a result of the modeling, our best estimate of the power-law slope for the inner halo (10 kpc $< R < R_{\rm Break}$) is $n_{\rm inner} = -2.78 \pm 0.02$ and for the outer halo ($R > R_{\rm Break}$) $n_{\rm outer} = -5.0 \pm 0.2$. We find $R_{\rm Break}$ is consistent with 45–50 kpc. The spatial density distribution for the model (reference model, as shown in Figure 9(b)) with these power-law slopes is shown in Figure 10. The outer slope and $R_{\rm Break}$ are consistent with the findings of K08. However, the inner slope is increased by ∼0.2. This is because K08 assumed ∼60% completeness for the inner halo while we found it to be 70%.

7. DISCUSSION

Our major findings are that the break in the RRL spatial density distribution found by K08 is indeed at $R \sim 45$ kpc with the power-law slope steepening from the inner (10 kpc $< R <$ 45 kpc) to the outer halo ($R \geqslant 45$ kpc).

Several previous studies support our results. We summarize a set of recent observational surveys of the density distribution in Table 5. Our results are similar to those of Watkins et al. (2009), who conducted an analysis of halo substructure traced by RRLs in SDSS Stripe 82, probing distances to ∼100 kpc. Sesar et al. (2010) performed an improved analysis of these data, using the same tracers, and compared the results with the smooth halo density profile of Jurić et al. (2008). They presented strong direct evidence that the halo stellar number density profile significantly

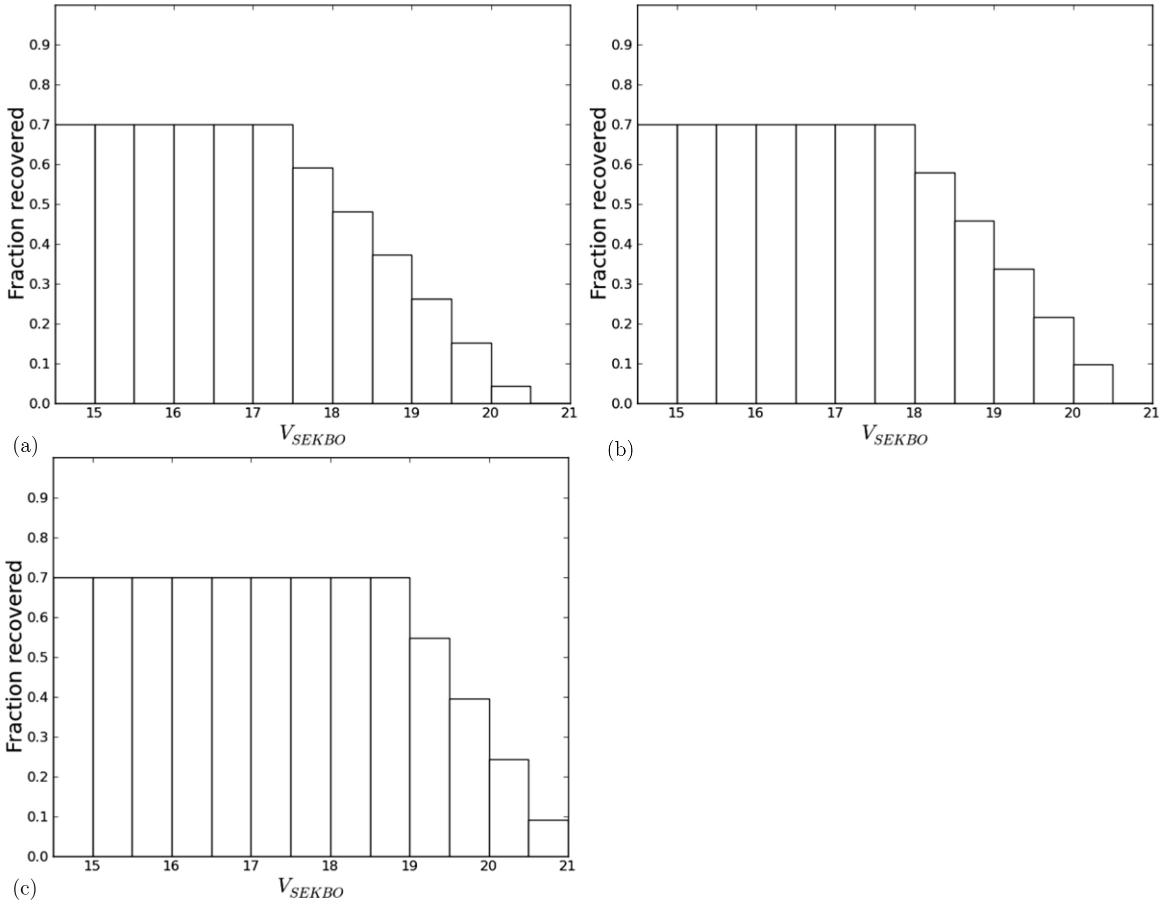

Figure 9. Completeness profile of RRL variables as a function of $V_{\rm SEKBO}$ magnitude: (a) Model1 with $V_{\rm Break} = 17$ and $V_{\rm Edge} = 20.2$, (b) Model14 (reference model) with $V_{\rm Break} = 17.5$ and $V_{\rm Edge} = 20.5$, and (c) Model40 with $V_{\rm Break} = 18.5$ and $V_{\rm Edge} = 20.8$. The completeness for each 0.5 mag bin is indicated.

Table 5
Power-law Index Results from Various Surveys

Reference	Project	Tracer	$R_{\rm Extent}$ (kpc)	$R_{\rm Break}$ (kpc)	$n_{\rm inner}$	$n_{\rm outer}$
Deason et al. 2011	SDSS DR-8	BHB and BSS	∼45	27	-2.30 ± 0.10	-4.60 ± 0.20
Sesar et al. 2011	CFHTLSD 170 sqdeg	Near-turn off MS	∼35	28	-2.62 ± 0.04	-3.8 ± 0.1
Sesar et al. 2010	SDSS STRIPE 82	RRLs and MS	∼100	∼30	...	Steepens significantly
de Jong et al. 2010	CMD Fitting to SEGUE	All relevant stars	30	30	-2.75 ± 0.07	...
Watkins et al. 2009	SDSS STRIPE 82	RRLs	∼100	23	−2.4	−4.5
Keller et al. 2008	SEKBO RRL Survey	RRLs	∼100	∼45	-2.48 ± 0.09	-5.0 ± 0.3
Jurić et al. 2008	SDSS	Near-turn off MS	∼20	...	−2.8	...
Bell et al. 2008	SDSS DR-5	MSTO	∼40	20	−2.0	−4.0
Miceli et al. 2008	LONEOS survey	RRLs	∼30	...	-2.43 ± 0.06	...
Sesar et al. 2007	SDSS STRIPE 82	RRLs	∼100	∼30	...	Steepens significantly
Bica et al. 2006	Harris' database (Harris 1996)	Globular Clusters	∼150	∼3.5	...	-3.9 ± 0.1
Wetterer & McGraw 1996	CTI survey	RRLs	∼80	25	-3.024 ± 0.077	Underdensity

steepens beyond a Galactocentric distance of ∼30 kpc. They also saw similar evidence in the distribution of the main-sequence stars to a radius of ∼40 kpc. Notably, the main-sequence stars are subject to different selection effects compared with RRLs and other horizontal branch (HB) stars, though these stars are much fainter ($Mv \sim +4$) than the HB stars ($Mv \sim +0.4$ to +0.8) and hard to detect at larger radii. Deason et al. (2011), using a large sample of blue HB and blue straggler stars (BSS) from SDSS DR-8, also found similar results.

However, De Propris et al. (2010) found that a single power law of index $R = -2.5 \pm 0.2$ matches the distribution of BHB stars within 100 kpc. While this power-law slope is similar to what other studies, including ours, suggest for the inner halo, it is definitely much shallower for the outer halo than the slope found here. De Propris et al. (2010) suggest that because the halo seems to have an abundance gradient (e.g., Carollo et al. 2007, 2010) and RRLs are potentially more metal rich than BHB stars, they are consequently more concentrated toward the Galactic center. Such an effect could result in the broken power law by reflecting that the stellar sample of De Propris et al. (2010) has lower overall metallicity at large distances. Although we agree that this would imply that the relative number

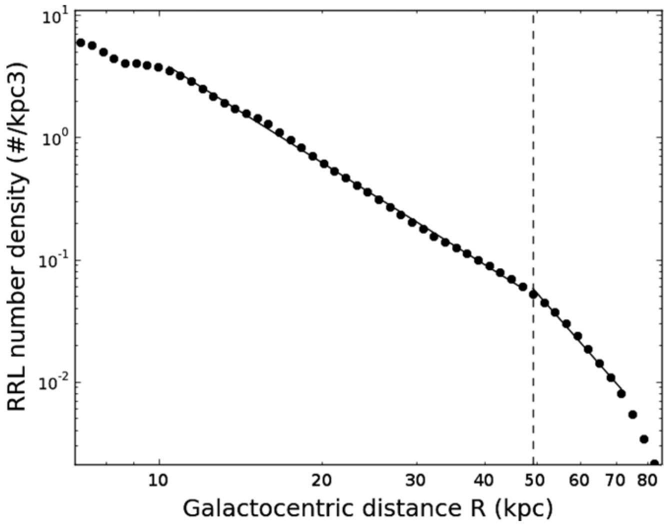

Figure 10. Space density distribution of RRLs for the reference model. The solid lines indicate the linear fits to the inner and the outer halos, and the dashed line indicates $R_{\rm Break} \sim 49$ kpc.

of RRLs decreases with increasing radius compared with BHB stars, this may not be the sole explanation for the steepening of the slope at larger radii as, in addition to metallicity, various other parameters such as age, He abundance, and mass loss, etc., also change the HB morphology (Lee et al. 1994; Catelan 2009, and references there in). It may be that RRLs are biased tracers at large radii and that their density distribution beyond the break radius ($R_{\rm Break}$) at ∼45–50 kpc is not representative of the overall density distribution of all halo stars at these large radii. To clarify this, we need to model how HB morphology responds to various parameters (e.g., metallicity and age gradients, etc.) over the entire Galactic halo. However, the variation of HB morphology is a complex process and such modeling is beyond the scope of this paper.

Theoretical studies also support the existence of a broken power law. The hydrodynamical cosmological simulations (GIMIC), out to ∼100 kpc and beyond, of Font et al. (2011) predict that there is a change in slope of the Galactic density profile. Their simulated mass density profile falls off as $n = -3.5$ at large radii $R > 30$ kpc. This is because the inner halo is dominated by in situ star formation, whereas the outer halo is primarily formed from many stellar accretion events (Zolotov et al. 2009; Zolotov 2011; Font et al. 2011). A number of other authors suggest that their observational results support this interpretation (e.g., Sesar et al. 2010; Carollo et al. 2007).

It is notable from Table 5 that the Watkins et al. (2009) and Sesar et al. (2010, 2007) studies have similar outer halo extent and have used the same tracer, RRLs, as in our current study. However, they found $R_{\rm Break} \leqslant 30$ kpc, while we found it between 45 and 50 kpc. Possible explanations for this difference include: (1) Stripe 82 contains large stellar overdensities and the two most significant substructures reside at $R \leqslant 40$ kpc containing almost 70% of the RRLs in Stripe 82 (more significantly the single substructure Herculus–Aquila–Cloud itself contains 60% of the RRLs; Watkins et al. 2009), and (2) Sesar et al. (2010) also drew a similar conclusion of clumpy nature and showed for $R \leqslant 30$ kpc there are regions of RRL overdensities while beyond 30 kpc there are underdensities. K08 also perceived clumpiness in the SEKBO distribution but in our study, we have focussed on the overall spatial distribution. We also stress here that we did not see any underdensity at $R \leqslant 30$ kpc, but beyond ∼45 kpc (Section 6). Again, Wetterer & McGraw (1996) also studied halo to a large extent (∼80 kpc) and both K08 and the present work used their technique to calculate the spatial distribution. Yet Wetterer & McGraw (1996) found $R_{\rm Break} \sim 25$ kpc. However, due to the small number of RRLs (only nine) at $R > 30$ kpc, the Wetterer & McGraw (1996) results at large radii are uncertain.

While the SEKBO survey covers a range of Galactic longitude and latitude (l, b), the actual area coverage is relatively limited (see Figure 4 of K08). Nevertheless, we have split up the full sample into a number of sub-samples in order to investigate possible variations in the break radius and power-law slopes with direction. Such investigations may reveal deviations from our assumed spherical symmetry. We note though that fluctuations from the smooth model have already been discussed in K08. We considered the following sub-samples: (a) two sub-samples, denoted by B_1 and B_2, one with $b > 0$ ($N_{\rm RRL} = 1150$) and the other with $b < 0$ ($N_{\rm RRL} = 866$) for all l; (b) two sub-samples, denoted by L_1 and L_2, one with $l > 270$ and $l < 90$ for all b ($N_{\rm RRL} = 1728$) and the other with $90 < l < 270$ for all b ($N_{\rm RRL} = 288$); and (c) four sub-samples with (i) $l > 270, l < 90$ and $b > 0$ ($N_{\rm RRL} = 965, L_1B_1$), (ii) $l > 270, l < 90$ and $b < 0$ ($N_{\rm RRL} = 763, L_1B_2$), (iii) $90 < l < 270$ and $b > 0$ ($N_{\rm RRL} = 185, L_2B_1$), and (iv) $90 < l < 270$ and $b < 0$ ($N_{\rm RRL} = 103, L_2B_2$). Here $N_{\rm RRL}$ is the number of RRL candidates in each sub-sample. For each sub-sample we then ran the 44 models (cf. Section 6) and compared the results with those for the entire sample. For the sub-sample L_2 and hence for the two sub-samples L_2B_1 and L_2B_2 there are insufficient RRL candidates for a meaningful analysis, but for the other five sub-samples we found break radii and outer power-law slopes consistent with those for the entire sample. However, we found that the sub-samples B_1 and L_1B_1 both had a steeper inner power-law slope ($n_{\rm inner} \sim -3.2$) than the equivalent sub-samples B_2 and L_1B_2, which had inner power-law slope values consistent with that for the overall sample (i.e., $n_{\rm inner} \sim -2.7$). The sub-sample L_1 also had inner power-law slope consistent with that for the total sample. We choose not to speculate on the possible reasons for this apparent difference in the inner power-law slope between the northern and southern Galactic hemispheres for the RRL space density distribution. A similar survey covering a significantly larger area of sky in both hemispheres is required to confirm or refute the apparent difference.

The outer halo is likely clumpy, patchy, and radially inhomogeneous with various stellar populations dominating different lines of sight. This occurs because the outer halo is not radially mixed due to the long orbital periods of the stars (Johnston et al. 1996; Mayer et al. 2002). Therefore, to avoid the significant influence of particular streams or clumps within a particular field of view, we need large sky area and deep photometric surveys to fully assess the overall density profile. The SkyMapper Survey (Keller et al. 2007) will help this situation. With its six-band filters and large field of view (5.7 deg^2), SkyMapper will provide a deep photometric survey of the whole southern hemisphere sky. Unlike any other survey, SkyMapper will have an extra "v" filter along with an enhanced "u" filter to measure the surface gravity for various stars (Keller et al. 2007). The three epoch observations together with appropriate color selection will help in identifying variable stars and in particular provide an ability to distinguish various classes of stars (RRLs, BHBs, main-sequence stars, BSSs, etc.). This will enable us to measure the radial density distribution of different stellar

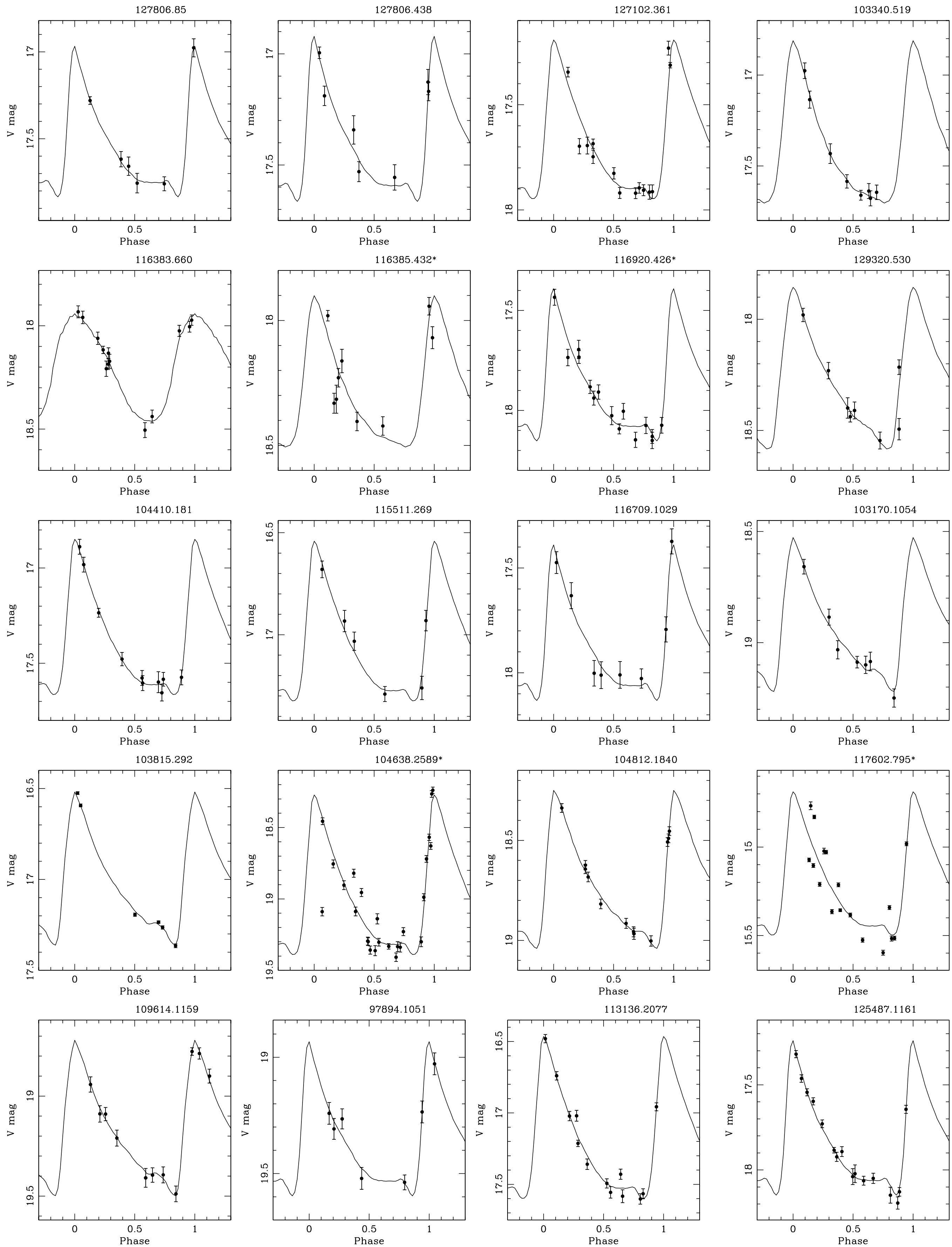

Figure A1. Final light curves for confirmed RR Lyraes (43 RRab and 11 RRc). Plots with "∗" are indicating Blazhko RRLs.

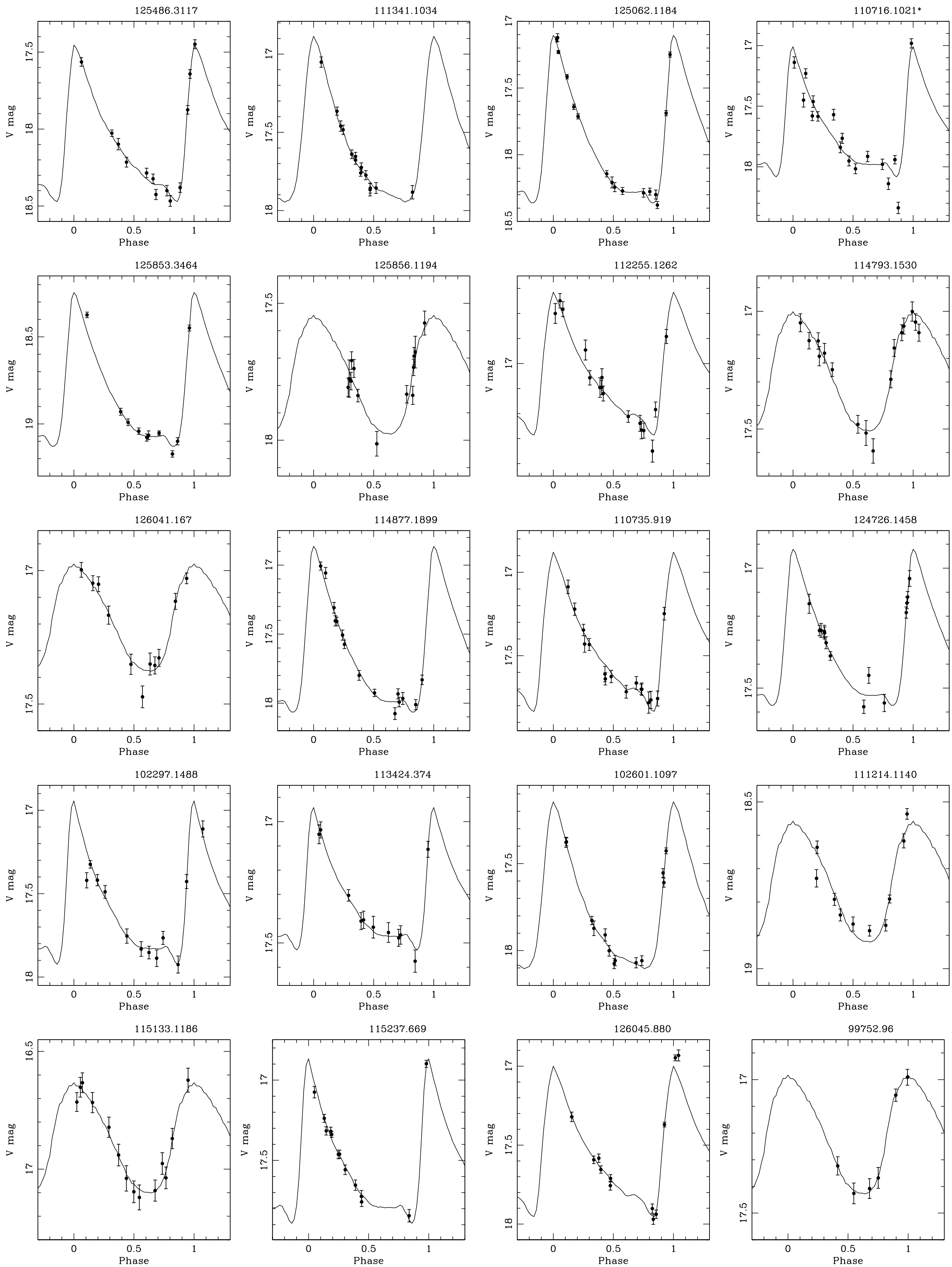

Figure A1. (Continued)

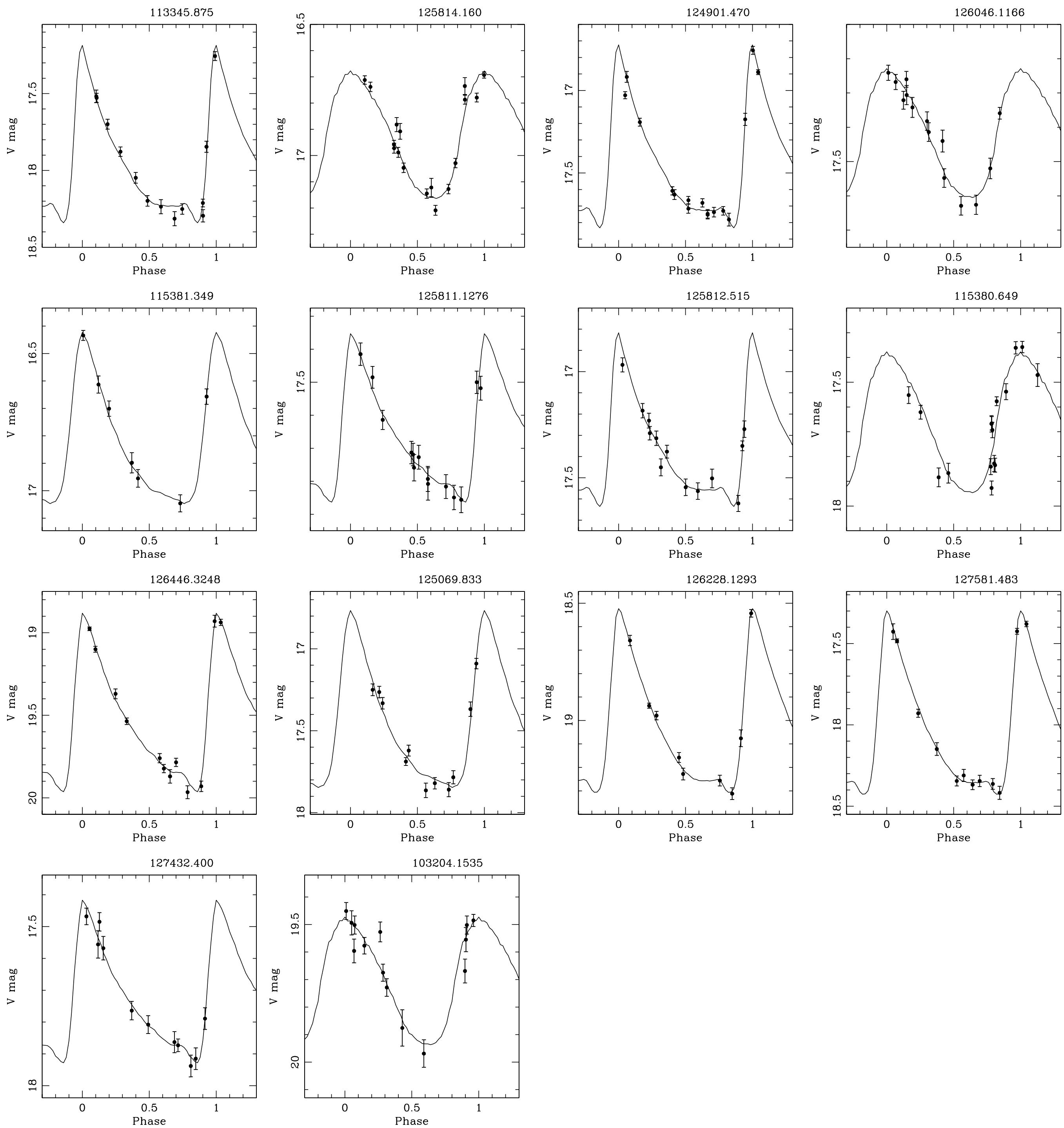

Figure A1. (Continued)

populations in the halo and to investigate whether the break radius is present for all halo populations. Thus, these new data, when available, will provide increased constraints on the formation of the galaxy's halo.

This paper uses observations obtained with ANU (The Australian National University) time on the Faulkes Telescopes (North and South) of the Las Cumbres Observatory Global Telescope Network. This research has been supported in part by the Australian Research Council through Discovery Project grant DP 0878137.

APPENDIX

APPENDIX MATERIAL

A.1. Table 6

A cross-match between the current data set and that of Prior et al. (2009) confirmed four objects as RRab. Of these, two were previously identified as undefined variables, one as non-variable and the other one as RRc. Object 116385.432 was identified as RRab by Prior et al. (2009). We find this star as a Blazhko RRab as we have two sets of observations separated by ∼100 days. These are given in Table 6. While calculating the completeness

Table 6
Objects Reidentified by Current Study from Prior et al. (2009)

Star ID	R.A. (J2000.0)	Decl. (J2000.0)	V_{SEKBO}	N_{Obs}[a]	N_{Obs}[b]	Star Type[a]	Star Type[b]	Period[a] (days)	Period[b] (days)	A_V[a]	A_V[b]
116709.1029	03 29 23.66	16 37 52.33	17.58	08	09	RRab	UV[c]	0.603	...	0.742	...
110735.919	21 14 25.80	−13 57 27.62	17.42	16	12	RRab	NV[d]	0.516	...	0.955	...
125812.515	21 48 49.46	−16 49 53.14	17.28	13	05	RRab	UV[c]	0.595	...	0.818	...
127806.438	00 25 23.38	−03 15 22.88	17.24	07	06	RRab	RRc	0.597	0.286	0.743	0.358
116385.432	02 10 44.39	12 45 09.71	17.88	09	08	Blazhko RRab	RRab	0.547	0.547	0.605	0.641

Notes.
[a] Found by current study.
[b] Confirmed by Prior et al. (2009).
[c] Undefined variables.
[d] Non-variables.

Table 7
Objects Identified from Prior et al. (2009)

Star ID	R.A. (J2000.0)	Decl. (J2000.0)	V_{SEKBO}	N_{Obs}[a]	N_{Obs}[b]	Star Type[a]	Star Type[b]	Period[a] (days)	Period[b] (days)	A_V[a]	A_V[b]
101751.216	02 11 41.33	03 29 41.10	15.03	09	06	RRc	NV[c]	0.347	...	0.377	...
104410.220	03 19 04.26	09 14 20.32	15.13	09	09	RRab	NV[c]	0.664	...	0.590	...
115213.329	03 23 36.23	14 47 54.25	15.50	12	05	RRab	RRab	0.625	0.625	0.505	...

Notes.
[a] Confirmed by Prior et al. (2009).
[b] Found by current study.
[c] Non-variables.

profiles, these objects were considered as RRab (Sections 3.4 and 5).

A.2. Table 7

This table presents two objects that were confirmed as RRLs by Prior et al. (2009), but could not be identified in this study due to insufficient observations. A third object 115213.329 is clarified as RRab with the help of Prior et al.'s (2009) catalog. We found the same period. However, we could not confirm the amplitude as we need more observations. We considered these three objects as RRLs in the completeness profile calculations, though we could not calibrate them photometrically.

A.3. Light Curves

Figure A1 shows the final light curves for the confirmed RRLs (43 RRab and 11 RRc). RRLs showing the Blazhko effect are noted with an asterisk following the variable name.

REFERENCES

Abadi, M. G., Navarro, J. F., & Steinmetz, M. 2006, MNRAS, 365, 747
An, D., Ramírez, S. V., Sellgren, K., et al. 2011, ApJ, 736, 133
Beers, T. C., Carollo, D., Ivezić, Ž., et al. 2012, ApJ, 746, 34
Bell, E. F., Zucker, D. B., Belokurov, V., et al. 2008, ApJ, 680, 295
Bica, E., Bonatto, C., Barbuy, B., & Ortolani, S. 2006, A&A, 450, 105
Blažko, S. 1907, Astron. Nachr., 175, 325
Bullock, J. S., & Johnston, K. V. 2005, ApJ, 635, 931
Carney, B. W. 1999, in ASP Conf. Ser. 165, The Third Stromlo Symposium: The Galactic Halo, ed. B. K. Gibson, R. S. Axelrod, & M. E. Putnam (San Francisco, CA: ASP), 230
Carollo, D., Beers, T. C., Chiba, M., et al. 2010, ApJ, 712, 692
Carollo, D., Beers, T. C., Lee, Y. S., et al. 2007, Nature, 450, 1020
Catelan, M. 2009, Ap&SS, 320, 261
Deason, A. J., Belokurov, V., & Evans, N. W. 2011, MNRAS, 416, 2903
de Jong, J. T. A., Yanny, B., Rix, H.-W., et al. 2010, ApJ, 714, 663
De Propris, R., Harrison, C. D., & Mares, P. J. 2010, ApJ, 719, 1582
Eggen, O. J., Lynden-Bell, D., & Sandage, A. R. 1962, ApJ, 136, 748
Font, A. S., McCarthy, I. G., Crain, R. A., et al. 2011, MNRAS, 416, 2802
Harris, W. E. 1996, AJ, 112, 1487
Ivezić, Ž., Sesar, B., Jurić, M., et al. 2008, ApJ, 684, 287
Ivezić, Ž., Vivas, A. K., Lupton, R. H., & Zinn, R. 2005, AJ, 129, 1096
Johnston, K. V., Hernquist, L., & Bolte, M. 1996, ApJ, 465, 278
Jordi, K., Grebel, E. K., & Ammon, K. 2006, A&A, 460, 339
Jurić, M., Ivezić, Ž., Brooks, A., et al. 2008, ApJ, 673, 864
Keller, S. C., Murphy, S., Prior, S., Da Costa, G., & Schmidt, B. 2008, ApJ, 678, 851
Keller, S. C., Schmidt, B. P., Bessell, M. S., et al. 2007, PASA, 24, 1
Kinman, T. D., Cacciari, C., Bragaglia, A., Buzzoni, A., & Spagna, A. 2007, MNRAS, 375, 1381
Landolt, A. U. 1992, AJ, 104, 340
Layden, A. C. 1998, AJ, 115, 193
Layden, A. C., Ritter, L. A., Welch, D. L., & Webb, T. M. A. 1999, AJ, 117, 1313
Lee, Y.-W., Demarque, P., & Zinn, R. 1994, ApJ, 423, 248
Mayer, L., Moore, B., Quinn, T., Governato, F., & Stadel, J. 2002, MNRAS, 336, 119
Miceli, A., Rest, A., Stubbs, C. W., et al. 2008, ApJ, 678, 865
Moody, R., Schmidt, B., Alcock, C., et al. 2003, Earth Moon Planets, 92, 125
Prior, S. L., Da Costa, G. S., Keller, S. C., & Murphy, S. J. 2009, ApJ, 691, 306
Saha, A. 1985, ApJ, 289, 310
Schlegel, D. J., Finkbeiner, D. P., & Davis, M. 1998, ApJ, 500, 525
Schönrich, R., Asplund, M., & Casagrande, L. 2011, MNRAS, 415, 3807
Searle, L., & Zinn, R. 1978, ApJ, 225, 357
Sesar, B., Ivezić, Ž., Grammer, S. H., et al. 2010, ApJ, 708, 717
Sesar, B., Ivezić, Ž., Lupton, R. H., et al. 2007, AJ, 134, 2236
Sesar, B., Jurić, M., & Ivezić, Ž. 2011, ApJ, 731, 4
Vivas, A. K., Zinn, R., Abad, C., et al. 2004, AJ, 127, 1158
Watkins, L. L., Evans, N. W., Belokurov, V., et al. 2009, MNRAS, 398, 1757
Wetterer, C. J., & McGraw, J. T. 1996, AJ, 112, 1046
Zolotov, A. 2011, BAAS, 43, 323.04
Zolotov, A., Willman, B., Brooks, A. M., et al. 2009, ApJ, 702, 1058